9.30.2021

Molecular structure and conformation of stereocilia tip-links elucidated by cryo-electron tomography

Johannes Elferich[1,2,3], Sarah Clark[1], Jingpeng Ge[1], April Goehring[1,3], Aya Matsui[1,3] and Eric Gouaux[1,3,4]

[1]Vollum Institute, Oregon Health & Science University, 3181 SW Sam Jackson Park Road, Portland, OR 97239

[2]RNA Therapeutics Institute, UMass Chan Medical School, 368 Plantation St, Worcester, MA 01605

[3]Howard Hughes Medical Institute, Portland, OR 97239

[4]Lead contact

[*]Correspondence: gouauxe@ohsu.edu

Abstract

Mechanosensory transduction (MT), the conversion of mechanical stimuli into electrical signals, underpins hearing and balance and is carried out within hair cells in the inner ear. Hair cells harbor actin-filled stereocilia, arranged in rows of descending heights, where the tips of stereocilia are connected to their taller neighbors by a filament composed of protocadherin 15 (PCDH15) and cadherin 23 (CDH23), deemed the 'tip-link'. Tension exerted on the tip-link opens an ion channel at the tip of the shorter stereocilia, thus converting mechanical force into an electrical signal. While biochemical and structural studies have provided insights into the molecular composition and structure of isolated portions of the tip-link, the architecture, location and conformational states of intact tip-links, on stereocilia, remains unknown. Here we report *in situ* cryo-electron microscopy imaging of the tip-link in mouse stereocilia. We observe individual PCDH15 molecules at the tip and shaft of stereocilia and determine their stoichiometry, conformational heterogeneity, and their complexes with CDH23. The PCDH15/CDH23 complexes occur in clusters, frequently with more than one copy of PCDH15 at the tip of stereocilia, suggesting that tip-links might consist of more than one copy of the PCDH15/CDH23 heterotetramer and by extension, might include multiple MT complexes.

Introduction

Vertebrates sense sound, movement and balance using specialized sensory neurons, called hair cells (McPherson, 2018). In mammals, hair cells are found in the inner ear and are organized in several specialized organs. Examples include the cochlea, which senses sound, and the utricle, which contributes to balance sensation (Ekdale, 2016). Hair cells harbor sensory microvili at their apical surface, which are called stereocilia. Stereocilia are rigid, due to being filled with crosslinked actin filaments (Tilney et al., 1992), and assemble in a staircase pattern in rows of descending height (Pickles et al., 1984). Upon deflection of the stereocilia staircase, tension is exerted on a filament connecting the tip of stereocilia with their taller neighbor, called the tip-link (Pickles et al., 1984). This tension then causes the opening of a channel, called the mechanosensory transduction (MT) channel, at the base of the tip-link (Zheng and Holt, 2021). The molecular mechanism of MT channel function, the conversion from mechanical to electrical signal in the inner ear, remains poorly understood.

The molecular nature of components of the MT machinery have been recently elucidated. The tip-link consists of the two-noncanonical cadherins protocadherin 15 (PCDH15) and cadherin 23 (CDH23) (Zheng and Holt, 2021). PCDH15 is situated at the tip of the shorter stereocilia and its two N-terminal cadherin domains bind to the two N-terminal cadherin domains of CDH23 (Kazmierczak et al., 2007; Sotomayor et al., 2012). The MT channel is likely formed by the transmembrane-channel like (TMC) protein 1 or 2 and the transmembrane protein of the inner ear (TMIE) (Zheng and Holt, 2021). PCDH15 assembles in the membrane together with lipoma HMGIC Fusion Partner-Like 5 (LHFPL5,TMHS) (Ge et al., 2018, p. 5) and pull-down studies using protein fragments suggest that PCDH15 may also interact with TMC-1 (Maeda et al., 2014). PCDH15 is also theorized to interact with the cytoskeleton via whirlin (Michel et al.,

2020), while TMC may be coupled to the cytoskeleton via CIB2 and ankyrin repeats (Tang et al., 2020). However, the molecular composition of the MT machinery and the 3D arrangements of each component remain unknown.

The fundamental transduction activity of the MT machinery is the conversion of force into an electrical signal (Hudspeth, 1989). Indeed, the mechanical displacement of the stereocilia can be modeled using Hooke's Law, suggesting the presence of an elastic element, or a 'gating spring', that couples displacement to the ion channel opening (Howard and Hudspeth, 1987). On the one hand, elasticity measurements of PCDH15 suggest that the tip-link itself acts as the gating-spring (Bartsch et al., 2019), while on the other hand the plasma membrane at the tip of stereocilia, as well as elements that couple the tip-link to the cytoskeleton, are other candidates to act as 'elastic elements' (Powers et al., 2012). Therefore, insights into the molecular structure and dynamics of the tip-link are essential for understanding mechanosensory transduction.

The molecular unit of the tip-link is a heterotetramer of PCDH15 and CDH23, where both cadherins form a parallel dimer (Dionne et al., 2018) and come together as a dimer-of-dimers using an anti-parallel 'handshake' of EC-1 and 2 of both cadherins (Sotomayor et al., 2012). The extracellular domains of both PCDH15 and CDH23 are a chain of cadherin domains with 11 and 27 repeats, respectively. Canonical cadherin domains form a 'stiff' dimer in the presence of calcium, due to stabilizing calcium binding sites in the linker regions between cadherin domains (Marquis and Hudspeth, 1997). Both PCDH15 and CDH23 have non-canonical linkers devoid of canonical calcium binding sites, thus likely promoting conformational mobility (Araya-Secchi et al., 2016; Jaiganesh et al., 2018; Powers et al., 2017). Notably, the linker between EC9 and EC10 of PCDH15 is flexible *in vitro,* allowing a bend of up to 90° (Araya-Secchi et al., 2016; Ge et al., 2018). Bending and extension along this linker has

been suggested as underlying the elasticity of the gating spring (Araya-Secchi et al., 2016), yet atomic force microscopy measurements and molecular dynamics simulations of PCDH15 also have suggested that individual cadherin domains can unfold to give rise to tip-link extension (De-la-Torre et al., 2018; Oroz et al., 2019). However, it is unclear which of these mechanisms occur *in situ.*

The majority of our current knowledge about the assembly of the tip-link *in situ* is based on fixed and stained scanning-electron microscopy (SEM) or freeze-fracture transmission electron microscopy (TEM) of stereocilia (Kachar et al., 2000; Michel et al., 2005). These images reveal a 120-170 nm long, helically coiled, filament with a diameter of 5 nm and a repeat of 40 nm (Kachar et al., 2000). Furthermore, these links appear to bifurcate at the upper and lower insertion sites into 2-3 individual strands, an observation that is difficult to reconcile in light of high resolution structural data showing that PCDH15 and CDH23 are parallel dimers and that both proteins also harbor membrane-proximal 'dimerization domains' (De-la-Torre et al., 2018; Dionne et al., 2018; Ge et al., 2018). This may be because the imaging methods relied on fixation and staining procedures, which are manipulations that can introduce artifacts or distortions.

More recently, cryo-electron microscopy imaging has been used to image stereocilia in their native state, avoiding these artifacts (Metlagel et al., 2019; Song et al., 2020). However, due to rapid damage of the specimen by high-energy electrons, the contrast of this imaging modality is low, making it challenging to visually identify relatively small features, such as the tip-link. Therefore, labeling approaches are required to unambiguously identify components of the MT machinery. In this study, we combine a stereocilia preparation technique for cryo-EM imaging (Metlagel et al., 2019; Song et al., 2020) with a highly specific, immuno-affinity labeling

approach using anti-PCDH15 antibody-coupled gold nanoparticles (AuNP) (Azubel et al., 2019) to elucidate the molecular structures and conformational states of tip-links, *in situ*, under native conditions.

Results

Cryo-CLEM imaging of immunolabeled stereocilia

To develop tools to identify PCDH15 in cryo-electron tomograms, we raised polyclonal antibodies (pAbs) against the entire extracellular region of mouse PCDH15. Immunostaining of mouse cochlea using these anti PCDH15 pAbs produces punctate features at the tips of stereocilia in hair cells derived from wild-type (WT) mice, features that are entirely absent from the stereocilia of PCDH15 knock-out mice, thus demonstrating the specificity and utility of the anti-PCDH15 pAbs (Figure 1A). We observed similar staining of stereocilia derived from mouse utricles, both in the presence of calcium and after chelation of calcium using BAPTA, indicating that the binding was independent of calcium and thus, also independent of the PCDH15-CDH23 'handshake' (Figure 1B). To facilitate the collection of a large dataset of tomograms focused on the tip-region of stereocilia, we adopted a stereocilia preparation technique in which the sensory epithelium is touched to holey carbon support film cryo-EM grids treated with poly-lysine, thus enabling the deposition of stereocilia onto the grid (Metlagel et al., 2019). We subsequently identified stereocilia by staining the sample with an actin dye and imaging with cryo-light fluorescence microscopy (Figure 1C), allowing us to estimate the number of squares with a favorable number of stereocilia and appropriate ice thickness. We then collected tomograms in these squares, focusing on positions where the tips of stereocilia coincided with holes in the holey carbon film (Figure 1C).

In initial experiments, we labeled stereocilia with the anti-PCDH15 pAbs using secondary antibodies conjugated to 5 nm gold particles. In the resulting images, we clearly visualized clusters of 5 nm gold particles in the images of some of the tips (Figure 1D). While this validated our immuno-labeling approach, we were unable to determine the number of PCDH15 molecules present due to the undefined stoichiometry of both the primary and secondary reagent. Furthermore, the gold particles obstructed the direct observation of the PCDH15 electron density.

Preparation of a PCDH15 gold-labeling reagent with 1:1 stoichiometry

To specifically label PCDH15 subunits with single gold particles, we developed a high affinity, slow off-rate ($k_{off} = 4.6 \times 10^{-5}$ 1/s), anti-PCDH15 monoclonal antibody (mAb), deemed 39G7. By examining the binding of 39G7 to a series of PCDH15 truncation constructs, we determined that the mAb binds to the EC3 cadherin domain, near the amino terminus (Figure 2A). Similar to the anti-PCDH15 pAbs, the 39G7 mAb stained PCDH15 on the surface of vestibular stereocilia, either in the presence or absence of calcium (Figure 2B).

To create a reagent to label PCDH15 subunits with a single gold particle, we created a 39G7 Fab construct with a single free cysteine residue at the C terminus of the heavy chain, thus enabling conjugation of the Fab to 3 nm AuNPs (Azubel et al., 2019, p. 2). Purification of the 39G7 Fab – AuNP complex via polyacrylamide electrophoresis and size exclusion chromatography (SEC) yielded a homogeneous species in which the Fab was a labeled with a single AuNP (Figure 2C+D), devoid of non AuNP-labeled Fabs. Using this reagent, we reasoned that we could directly count PCDH15 subunits because only a single Fab will bind to each PCDH15 subunit and each Fab is labeled by a single AuNP. We confirmed this prediction by forming a complex between the 39G7 Fab – AuNP and recombinant PCDH15, isolating the

complex by SEC (Figure 2E) and imaging the complex by single particle cryo-EM (Figure 2F). On micrographs and tomographic reconstructions (Movie S1), we clearly identified pairs of AuNPs bound to the PCDH15 extracellular domain, consistent with a dimeric model of the PCDH15 extracellular domain, the 39G7 Fab binding to EC3 and the ability of the Fab – AuNP complex to allow us to identify and count PCDH15 subunits.

39G7-AuNP labeling of stereocilia shows that PCDH15 is a dimer

We prepared cryo-EM grids using utricles stained with 39G7 Fab-AuNP and collected tomograms, primarily of stereocilia tips (Figure 3E). On approximately half of the tomograms we identified 3 nm gold particles within ~38 nm of the stereocilia membrane, a distance that is consistent with the binding of 39G7 to ECD3 of PCDH15. We also identified AuNP labels in tomograms of the stereocilia shaft region, but only in about a third of the tomograms that featured only stereocilia shaft regions. Close inspection of the electron density around the AuNPs frequently revealed ~50 nm long filamentous density consistent with the extracellular domain of PCDH15 (Figure 3A-B, Movie S2-3). In tomograms with relatively thin ice (<200 nm) and an appropriate orientation of the filament to the tilt-axis, dimeric features of the PCDH15 domain are evident that, together with the presence of the AuNP pairs with a distance of 20 nm, demonstrates that PCDH15 forms a dimer *in situ.* In some cases, we observed individual gold particles instead of a pair of AuNPs (Figure 3C-D, Movie S4-5) yet also dimeric features associated with PCDH15 chain, thus indicating that the visualization of individual AuNPs was likely due to incomplete labeling of PCDH15 and not the presence of PCDH15 monomers. We quantified the occurrence of AuNP dimers and monomers (Figure 3F) and found a ratio of 3:1. Under the assumption that bindings of the 39G7 Fab to either protomer are independent events, we can use this ratio to estimate the fraction of PCDH15 protomers labeled with 39G7-AuNP

(0.86) and the fraction of PCDH15 dimers that are completely unlabeled (0.02). While this may be an underestimation of the number of unlabeled PCDH15 molecules, either due to cooperativity of 39G7 binding or due to air-water interface effects, it nevertheless demonstrates that the 39G7 Fab-AuNP robustly labels PCDH15 *in situ* and therefore allows precise quantification of the number of PCDH15 molecules at the tips of stereocilia.

Stereocilia tips harbor multiple copies of PCDH15

We carefully quantified the number of PCDH15 molecules in all imaged stereocilia tips (n=396) (Figure 4F). Slightly more than half of the stereocilia tips (58%) did not contain a PCDH15 label. While this could be due to an underestimate of the labeling efficiency or due to preferential selection of stereocilia in the tallest row, we believe the most likely explanation is damage to stereocilia tips during the blotting of stereocilia on the cryo-EM grids. In some cases (5.8%), we found PCDH15 molecules in the shaft region just 'below' the stereocilia tips (Figure 4A, Movie S6). It is possible that these molecules were initially located on the tip, but diffused away in the time between applying tissue to the grid and plunge-freezing. In 13% of tips we found a single molecule of PCDH15 at the tip (Figure 4B+C, Movie S7-8), similar to commonly depicted models of the MT complex. However, in almost twice the number of stereocilia tips (23%) we found multiple copies of PCDH15 at the tip, either clustered at the tip (Figure 4D, Movie S9) or spread across its surface (Figure 4E, Movie S10). Because we cannot determine that maturity of the hair cells from which the stereocilia are derived, multiple PCDH15 molecules at the tips may be due to stereocilia derived from immature hair cells. Indeed, many molecular models of the MT machinery posit the presence of one copy of the PCDH15 dimer bound to a single MT-channel. Our data, however, suggests that many tips might harbor multiple

194 copies of the MT machinery, which in turn might underly variation in the ion channel
195 conductance at individual tips (Beurg et al., 2018).

196 **Tomographic reconstructions of PCDH15-CDH23 heterotetramers**

197 In a few tomograms, we found electron-density extending beyond the tip of PCDH15,
198 consistent with a 120 nm long filament inserted into two distinct membranes (Figure 5). While
199 we cannot determine the molecular identity of this density unambiguously, the dimensions of this
200 molecule suggest that the density corresponds to CDH23. In one example, we found a stereocilia
201 tip with 5 copies of a PCDH15 dimer, 3 of which were connected to a putative CDH23 density,
202 which in turn was inserted into a small spherical liposome (Figure 5A, Movie S11). Our
203 interpretation of this structure is that this was a tip-link assembly, disrupted during sample
204 preparation, where a portion of the membrane surrounding CDH23 was 'torn off' of the
205 neighboring stereocilia, yielding CDH23 bound to a liposome. In another case, a cluster of five
206 PCDH15 molecules close to a stereocilium tip is connected to four CDH23 densities inserted into
207 a lipid membrane fragment (Figure 5B, Movie S12).
208 We also observed structures in which it appears as though PCDH15, together with a fraction of
209 surrounding membrane, were extracted from the shorter stereocilium (Figure 5C+D, Movie S13-
210 14). In both cases we found 3-5 copies of PCDH15 and CDH23. The fact that we observed most
211 PCDH15/CDH23 complexes in structures that appear to be the result of partial damage of the
212 tip-link, is consistent with the earlier interpretation of the missing PCDH15 label is due to
213 damaged tip-links. It is also possible that clusters of PCDH15/CDH23 complexes are more stable
214 than isolated PCDH15/CDH23 complexes, and thus more frequently observed.
215
216

An intact tip-link surrounded by non CDH23-bound PCDH15 molecules

In one tomogram, we imaged the tip of a stereocilium situated next to a longer stereocilium (Figure 6A, Movie S15). While we observed 17 AuNPs at the tip of the shorter stereocilium, we only unambiguously identified the density for four PCDH15 molecules. On one of these PCDH15 molecules we observed a 120 nm long filament, connecting PCDH15 to the longer stereocilium (Figure 6B). We hypothesize that this is most likely an intact tip-link. Upon closer inspection (Figure 6C), we can clearly identify dimeric features on this PCDH15 molecule. Other adjacent PCDH15 molecules are also clearly dimeric entities (Figure 6D), yet are not bound to CDH23. Further down the two stereocilia we identified another copy of PCDH15, apparently connected via CDH23 to the other stereocilium (Figure 6E). In this case PCDH15 appears to be bent, by about 90º, at juncture of the EC9-EC10 cadherin domains, a 'joint' between cadherin domains that has previously been identified as flexible in cryo-EM and crystallography structures of PCDH15 extracellular domain constructs (Araya-Secchi et al., 2016; Ge et al., 2018). We speculate that this link may be in the process of being trafficked to the tip and that the EC9-EC10 bend helps to accommodate the long filament within the relatively narrow space between stereocilia.

Lateral links consisting of PCDH15/CDH23

While in the majority of tomograms we identified 10 or fewer copies of PCDH15, several tomograms exhibit numbers of labels consistent with hundreds of copies of PCDH15. In the most striking example (Figure 7A, Movie S16), we observed these labels between stereocilia that appear thinner and less densely packed with actin than other stereocilia. In this tomogram we counted 309 AuNPs and modeled 56 PCDH15 molecules in cases where we observed the corresponding electron density. Many of the PCDH15 molecules are involved in links to

neighboring stereocilia, via a 120 nm filament, which again is likely CDH23. We observed density for 20 putative CDH23 molecules, molecules which likely participate in the 'lateral links' which form early in development of stereocilia bundles and are composed of PCDH15 and CDH23 (Michel et al., 2005). Inspection of the densities shows that multiple copies of CDH23 cluster together, primarily via the N-terminal half of CDH23, so as to obscure identification of individual stands (Figure 7B+C). We speculate that these clusters might have given rise to the appearance of single tip-links with multiple upper and lower insertion points in stained EM images. Furthermore, we find examples of CDH23 that appear bent half-way between the N- and C-termini, indicating that CDH23 might also have a flexible cadherin domain 'joint', similar to the EC9-EC10 interface of PCDH15 (Figure 7D). A potential candidate for this joint is the non-canonical linker between EC12 and EC13 of CDH23 (Jaiganesh et al., 2018).

Discussion

The combination of cryo-EM and AuNP labeling provides a molecular resolution view of the structure, stoichiometry, and organization of tip-links in their native environment. This work is the first look at native tip-links *in situ*, as previous studies relied on microscopy of fixed and stained specimens, which have an inherently lower resolution and are prone to artifacts (Indzhykulian et al., 2013; Kachar et al., 2000; Michel et al., 2005).

We observe clusters of PCDH15-CDH23 complexes on the stereocilia tip and shaft, as well as multiple copies of PCDH15 at stereocilia tips, ranging from two to more than five. Because the majority of the PCDH15 molecules we observed were not bound to CDH23 to form an intact tip-link, the mechanistic underpinnings of multiple PCDH15 molecules, if any, are unclear. One possibility is that each PCDH15 molecule was coupled to a functional MT channel and the tip-link was ruptured during cryo-EM grid preparation. This would imply that there are

multiple MT complexes per stereocilia tip, as suggested previously (Beurg et al., 2018). Confocal microscopy images of stereocilia expressing mCherry-tagged TMC1 indicate that there are an average of 7.1 TMC1 channels per stereocilia tip derived from the inner hair cells of P4 aged mice. The number of TMC1 per stereocilia tip varies from four to twenty depending on the cochlear localization, mirroring the high degree of variability we observed for PCDH15.

It is also possible that a large number of PCDH15 molecules may be necessary for rebinding to CDH23 in the event of tip-link breakage. Atomic force microscopy experiments indicate that the lifetime of the PCDH15-CDH23 bond is only ~8 seconds at resting tension, suggesting that the tip-link is a highly dynamic connection (Mulhall et al., 2021). A pool of nearby PCDH15 molecules may enable fast recovery after tip-links are broken. It has also been suggested that intermediate PCDH15-PCDH15 tips form first during tip-link regeneration, followed by mature PCDH15-CDH23 tip-links, necessitating the presence of multiple PCDH15 molecules (Indzhykulian et al., 2013).

Our tomograms also revealed distinct structural features of PCDH15 and CDH23. Most intact tip-links were approximately straight, ~120 nm length PCDH15-CDH23 heterotetramers consisting of a PCDH15 dimer joined to a CDH23 dimer. However, in several tip-links, we observed a ~90^{o} bend in PCDH15 or CDH23. PCDH15 is bent at approximately the EC9-EC10 interface, which has been identified as flexible in cryo-EM and crystal structures of recombinant PCDH15, while CDH23 appears to be bent near EC13. Crystal structures of CDH23 identified non-canonical linker regions and altered Ca^{2+} binding sites within this region, motifs that could confer increased flexibility (Jaiganesh et al., 2018). Furthermore, we often observe a ‘splitting’ of the CDH23 dimer at various points, most frequently at the C-terminal end. This type of structural heterogeneity is not observed for PCDH15. Crystallography studies of CDH23 have

noted a curious lack of multimerization interfaces between CDH23 protomers, consistent with our observations, yet a rationale for minimal interchain CDH23 interactions remains to be determined (Jaiganesh et al., 2018), other than to reduce likelihood of CDH23 aggregation.

In selected stereocilia, we note that the high densities of lateral PCDH15-CDH23 links are consistent with our capture of an immature hair bundle. While the utricles employed in our study were isolated from P6-9 mice, lateral links are still present until approximately P9 (Goodyear et al., 2005). These extensive lateral links stabilize the stereocilia during the early stages of development by acting as a cohesive tethers, gradually being pruned until only the tip-link remains in a mature hair bundle (Boëda et al., 2002; Michel et al., 2005).

Our work highlights the power of gold immunolabeling and cryo-EM to study rare protein complexes. The MT complex is notorious for its low abundance, conspiring to make studies of the mechanism of MT channel gating by tip-link tension challenging. The images presented here reveal structural features of the MT machinery and demonstrate that the employed techniques can be used to visualize single molecules in their native environment. It will be exciting to use this technique to explore additional components of the MT complex, including TMC1 and TMIE, in order to define their locations, stoichiometries and structures within the architecture of the MT machinery.

Methods

PCDH15 EC1-EL expression and purification

A gene encoding the amino acid sequence of the mouse PCDH15 extracellular region (Uniprot entry Q99PJ1), from the first cadherin domain (EC1) to the membrane-proximal ‘EL’ domain (PCDH15 EC1-EL), was synthesized and cloned into a pBacMam vector (Goehring et al., 2014), and included a C-terminal yellow fluorescent protein (YFP) fluorophore followed by a

polyhistidine tag. This construct was used to generate baculovirus, which was then employed to infect HEK293 cells as previously described (Goehring et al., 2014). Approximately 96 hours after viral transduction, the cell medium was harvested and the secreted PCDH15 EC1-EL protein was isolated by metal ion affinity chromatography, and further purified by size exclusion chromatography (SEC) in TBS Buffer (20 mM Tris pH8, 150 mM NaCl). The final material was concentrated to ~ 2mg/ml, aliquoted and stored at -80 ºC.

Antibody generation

Rabbit polyclonal and monoclonal antibodies were generated using standard techniques by Genscript using the soluble PCDH15 EC1-EL extracellular region as the antigen. Polyclonal serum was used to isolate antibodies using affinity-purification with the PCDH15 EC1-EL extracellular domain. Hybridoma supernatants were screened against the PCDH15 EC1-EL antigen in the presence and absence of 1 mM calcium to identify clones that recognize the calcium-bound and apo forms of the protein. Supernatants that tested positive by ELISA were further screened by fluorescence detection chromatography (FSEC) and Western blot and the clone 39G7 was sequenced and monoclonal antibody was produced recombinantly.

Immunofluorescence

Cochlea and utricles were dissected from mice at ages P6-9 in DMEM/F12 media (Gibco). The tissue was incubated for 30 minutes in 10 ug/ml of indicated antibody in DMEM/F12 media, followed by washing, 3 times for 10 minutes each, in the same media. Where indicated, 5 mM BAPTA was included in staining and washing media to chelate calcium. The tissue was next fixed with in a buffer composed of 4% paraformaldehyde in phosphate-buffered saline (PBS) for 10 minutes. After 3 washes in PBS, the tissue was permeabilized and blocked using PBS with 0.1% Triton X-100, 5% bovine serum albumin (BSA), and 10%

standard goat serum. Subsequently, the tissue was stained with goat-anti-rabbit antibodies fused to Alexa-594 and phalloidin fused to Alexa-405. After 3 washes with PBS, the tissue was mounted with Vectashield mounting media and imaged using a Zeiss LSM 980 confocal microscope using a 63x/1.49 NA objective.

AuNP generation

A solution of 84 mM 3-mercaptobenzoic acid (3-MBA) in methanol was mixed with a 28 mM solution of $HAuCl_4$ in methanol at 7:1 molar ratio, followed by 2.5 volumes of water. The pH was adjusted by adding concentrated aqueous NaOH to a final concentration of 100 mM. This solution was mixed by end-over-end rotation for at least 16 hours. Afterwards, the solution was diluted with 27% methanol to achieve a final concentration of 2.5 mM 3-MBA. $NaBH_4$ was added to a final concentration of 2 mM using a fresh 150 mM stock solution prepared in 10 mM NaOH. After mixing for 4.5 hours, the gold particles were precipitated by adjusting the NaCl concentration to 100 mM and by adding methanol to a final concentration of 70%. Gold AuNPs were pelleted by centrifugation at 5,000 rpm for 20 minutes and washed with 70% methanol. The pellet was dried overnight in a desiccator and re-suspended in water.

An expression construct for a Fab' fragment of 39G7 was designed using a dual-promoter Sf9-expression plasmid (Vectorbuilder). For the 39G7 light chain, we replaced the native signal peptide with the GP64 signal peptide and inserted the coding sequence downstream of the pH promoter. For the 39G7 heavy chain, we replaced the native signal peptide with the GP64 signal peptide and truncated the coding sequence after G256, thereby removing the Fc fragment but retaining C243 and C248 at the C-terminus. The coding sequenced was then inserted after the P10 promoter and fused with a histidine tag at the C-terminus. The 39G7 Fab' was expressed in Sf9 cells for 96 hours at 27 ^{o}C. The media was adjusted to pH 8, cleared by centrifugation and

355 then concentrated to about 100 ml using a tangential-flow concentrator. The concentrated media
356 was pumped over a 5 ml metal ion affinity column, equilibrated with PBS. The column was
357 washed extensively with PBS supplemented with 30 mM imidazole and Fab' was eluted with
358 PBS supplemented with 500 mM imidazole. The yield was 2 mg of Fab' per liter of culture. The
359 pooled fractions were concentrated to 5 mg/ml and aliquots were plunge-frozen in liquid
360 nitrogen and stored at -80 ºC.

361 To conjugate the Fab to the AuNPs, an aliquot of 39G7 Fab' was thawed and incubated
362 with 2 mM tris (2-carboxyethyl) phosphine hydrochloride (TCEP) for 1 hour at 37 ºC. After
363 clarification by ultracentrifugation, the 39G7 Fab was applied to a SEC column equilibrated with
364 TBE buffer (100 mM Tris, 100mM boric acid, 2mM EDTA). The peak fractions were
365 concentrated immediately to 2 mg/ml and a test conjugation was set up at different molar ratios
366 of Fab' and AuNP (4:1,2:1,1:1,1:2,1:4). After a 30-minute incubation at 37 ºC, the reactions were
367 analyzed on a 12.5% PAGE gel made with TBE and 10% glycerol. The condition with the
368 highest yield of the 1:1 AuNP/Fab complex was chosen for large scale conjugation. To coat the
369 AuNPs with PEG, the conjugate was immediately separated on a PAGE gel following and 1:1
370 39G7:AuNP recovered in TB buffer. After concentration, 1 mM of mPEG550-SH was added and
371 incubated for 60 minutes at 37 ºC. The conjugate was then purified by SEC using a Superose 6
372 column equilibrated with PBS. Fractions corresponding to 39G7-AuNP conjugate were pooled,
373 concentrated to 1 μM (assuming an extinction coefficient of $3x10^6$ (M^{-1} cm^{-1}) at 500 nm) and
374 stored at 4 ºC.

Grid preparation

Utricles were dissected from P8-P11 mice in DMEM/F12 buffer. Otoconia were removed using an eyelash. Utricles were incubated for 30 minutes in DME M/F12 containing 100 nM 39G7-AuNP and 500 nM SirActin and then washed three times for 5 minutes in DMEM/F12. Utricles were then placed stereocilia-side down on C-Flat 200 mesh copper grids with a 2/1 spacing carbon film that were pretreated with 0.1 mg/ml poly-D-lysine and suspended in 20 ul drops of DMEM/F12. After 2-3 seconds, the utricle was removed and placed on another region of the grid for up to three times. The grid was removed 'edge-first' from the drop and excess liquid was removed by touching the edge to a piece of Whatman No. 40 filter paper. A 2.5 ul drop of DMEM/F12 containing 0.05% fluorinated octyl-maltoside and 10 nm highly uniform gold fiducials at an OD_{500} of roughly 5.0 were added to the grid. The grid was then placed on a manual blotting apparatus and excess solution was removed by placing a 595 filter paper (TED-Pella) for 6-10 seconds to the side of the grid without sample. Afterwards, the grid was rapidly plunged into a mixture of ethane and propane cooled to liquid nitrogen temperature. Grids were imaged in a CMS196 cryostage (Linkam) on a LSM880 confocal microscope (Zeiss) using the AiryScan detector. Grids that did not exhibit SirActin fluorescence in multiple squares**,** or had excessive damage to the carbon support**,** were discarded.**Tilt-series acquisition**

Tilt-series of the recombinant PCDH15 ECD1-EL extracellular region labeled with the 9G7-AuNP was acquired using a Thermo Fisher Arctica microscope operated at 200 keV, without an energy filter, on a Gatan K3 detector. Tilt-series of stereocilia were obtained on a Thermo Fisher Krios microscope operated at 300 keV with an energy filter on a Gatan K3 detector. A subset of tomograms were obtained from a Krios microscope also equipped with a spherical aberration corrector.

In all cases, tilt-series were obtained from -60 to 60 degrees using a 3-degree interval using SerialEM. Data was either acquired by sweeping from -30 to 60 degrees and then from -30 to -60 degrees or by using a grouped dose symmetric scheme. In all cases the total electron dose was 80-120 e-/A^2. Defocus was varied between -2.5 and -4.0 um.

Tomography processing

Tomograms were reconstructed using the IMOD program (Mastronarde and Held, 2017), employing the 10 nm gold fiducials for alignment. In some cases, the 3 nm AuNP label was also included as a fiducial. The tilt series was binned by 4 to a final pixel size of 6.6 A, CTF corrected, the 10 nm gold particles were subtracted, and the tilt-series was dose-weighted. Tomograms were reconstructed using a SIRT-like filter with 8 iterations. In cases where a substantial amount of sample deformation was observed, tomograms were reconstructed using the tomoalign program (Fernandez et al., 2019), using polynomials and the 'thick' preset. If indicated, tomograms were denoised using the denoise3d model of Topaz (Bepler et al., 2020).

Tomogram annotation

Membranes were annotated manually in XY slices using the 3dmod program (Kremer et al., 1996). Actin filaments were manually annotated in 26.4 nm thick slices perpendicular to the stereocilium length. AuNP nanoparticles were either manually annotated or annotated using the findbeads3d program of the IMOD suite. PCDH15 was positioned by identifying the membrane insertion point and the PCDH15 tip in the 'Slicer' windows of the 3dmod program. The density of the PCDH15 model was then aligned along these two points and, in some cases, was rotated until the projection matched the density visible in the slicer window. Actin filaments were manually annotated in slices perpendicular to the stereocilia axis using 3dmod. A low-pass filtered electron-density of actin was placed along the annotated filaments using the

clonevolumes program. The final render of each model was performed using USCF ChimeraX (Pettersen et al., 2021).

Data availability

Tomograms depicted in the figures have been deposited in the EMDB under accession codes EMD-25046, EMD-25047, EMD-25048, EMD-25049, EMD-25050, EMD-25051, EMD-25052, EMD-25053, EMD-25054, EMD-25055, EMD-25056, EMD-25057, EMD-25058, EMD-25059, EMD-25060, and EMD-25061 (in order of appearance). The corresponding tilt-series have been deposited in EMPIAR under accession code EMPIAR-10820. Other raw data is available from the authors upon request.

Acknowledgments

We would like to thank the staff at the Pacific Northwest Center of Cryo-EM and at the Janelia Cryo-Electron Microscopy facility for help with data collection. We also would like to thank Lauren-Ann Metskas, Eileen O'Toole, and Songye Chen for instructions for tomography data acquisition and data processing. We would like to thank Maia Azubel for helpful discussions about AuNP synthesis and conjugation. Furthermore, we would like to thank Lori Vaskalis for assistance in preparing figures and Rashell Hallford for careful editing of the manuscript. E.G. is the Bernard and Jennifer LaCroute Chair in Neuroscience and an investigator with the Howard Hughes Medical Institute.

References

Araya-Secchi R, Neel BL, Sotomayor M. 2016. An elastic element in the protocadherin-15 tip link of the inner ear. *Nat Commun* **7**:13458. doi:10.1038/ncomms13458

Azubel M, Carter SD, Weiszmann J, Zhang J, Jensen GJ, Li Y, Kornberg RD. 2019. FGF21 trafficking in intact human cells revealed by cryo-electron tomography with gold nanoparticles. *eLife* **8**:e43146. doi:10.7554/eLife.43146

Bartsch TF, Hengel FE, Oswald A, Dionne G, Chipendo IV, Mangat SS, El Shatanofy M, Shapiro L, Müller U, Hudspeth AJ. 2019. Elasticity of individual protocadherin 15

447 molecules implicates tip links as the gating springs for hearing. *Proc Natl Acad Sci U S A*
448 **116**:11048–11056. doi:10.1073/pnas.1902163116
449 Bepler T, Kelley K, Noble AJ, Berger B. 2020. Topaz-Denoise: general deep denoising models
450 for cryoEM and cryoET. *Nat Commun* **11**:5208. doi:10.1038/s41467-020-18952-1
451 Beurg M, Cui R, Goldring AC, Ebrahim S, Fettiplace R, Kachar B. 2018. Variable number of
452 TMC1-dependent mechanotransducer channels underlie tonotopic conductance gradients
453 in the cochlea. *Nat Commun* **9**:2185. doi:10.1038/s41467-018-04589-8
454 Boëda B, El-Amraoui A, Bahloul A, Goodyear R, Daviet L, Blanchard S, Perfettini I, Fath KR,
455 Shorte S, Reiners J, Houdusse A, Legrain P, Wolfrum U, Richardson G, Petit C. 2002.
456 Myosin VIIa, harmonin and cadherin 23, three Usher I gene products that cooperate to
457 shape the sensory hair cell bundle. *EMBO J* **21**:6689–6699. doi:10.1093/emboj/cdf689
458 De-la-Torre P, Choudhary D, Araya-Secchi R, Narui Y, Sotomayor M. 2018. A Mechanically
459 Weak Extracellular Membrane-Adjacent Domain Induces Dimerization of Protocadherin-
460 15. *Biophys J* **115**:2368–2385. doi:10.1016/j.bpj.2018.11.010
461 Dionne G, Qiu X, Rapp M, Liang X, Zhao B, Peng G, Katsamba PS, Ahlsen G, Rubinstein R,
462 Potter CS, Carragher B, Honig B, Müller U, Shapiro L. 2018. Mechanotransduction by
463 PCDH15 Relies on a Novel cis-Dimeric Architecture. *Neuron* **99**:480-492.e5.
464 doi:10.1016/j.neuron.2018.07.006
465 Ekdale EG. 2016. Form and function of the mammalian inner ear. *J Anat* **228**:324–337.
466 doi:10.1111/joa.12308
467 Fernandez J-J, Li S, Agard DA. 2019. Consideration of sample motion in cryo-tomography
468 based on alignment residual interpolation. *J Struct Biol* **205**:1–6.
469 doi:10.1016/j.jsb.2019.01.005
470 Ge J, Elferich J, Goehring A, Zhao H, Schuck P, Gouaux E. 2018. Structure of mouse
471 protocadherin 15 of the stereocilia tip link in complex with LHFPL5. *eLife* **7**:e38770.
472 doi:10.7554/eLife.38770
473 Goehring A, Lee C-H, Wang KH, Michel JC, Claxton DP, Baconguis I, Althoff T, Fischer S,
474 Garcia KC, Gouaux E. 2014. Screening and large-scale expression of membrane proteins
475 in mammalian cells for structural studies. *Nat Protoc* **9**:2574–2585.
476 doi:10.1038/nprot.2014.173
477 Goodyear RJ, Marcotti W, Kros CJ, Richardson GP. 2005. Development and properties of
478 stereociliary link types in hair cells of the mouse cochlea. *J Comp Neurol* **485**:75–85.
479 doi:10.1002/cne.20513
480 Howard J, Hudspeth AJ. 1987. Mechanical relaxation of the hair bundle mediates adaptation in
481 mechanoelectrical transduction by the bullfrog's saccular hair cell. *Proc Natl Acad Sci*
482 **84**:3064–3068. doi:10.1073/pnas.84.9.3064
483 Hudspeth AJ. 1989. How the ear's works work. *Nature* **341**:397–404. doi:10.1038/341397a0
484 Indzhykulian AA, Stepanyan R, Nelina A, Spinelli KJ, Ahmed ZM, Belyantseva IA, Friedman
485 TB, Barr-Gillespie PG, Frolenkov GI. 2013. Molecular remodeling of tip links underlies
486 mechanosensory regeneration in auditory hair cells. *PLoS Biol* **11**:e1001583.
487 doi:10.1371/journal.pbio.1001583
488 Jaiganesh A, De-la-Torre P, Patel AA, Termine DJ, Velez-Cortes F, Chen C, Sotomayor M.
489 2018. Zooming in on Cadherin-23: Structural Diversity and Potential Mechanisms of
490 Inherited Deafness. *Struct Lond Engl 1993* **26**:1210-1225.e4.
491 doi:10.1016/j.str.2018.06.003

Kachar B, Parakkal M, Kurc M, Zhao Y, Gillespie PG. 2000. High-resolution structure of hair-cell tip links. *Proc Natl Acad Sci U S A* **97**:13336–13341. doi:10.1073/pnas.97.24.13336

Kazmierczak P, Sakaguchi H, Tokita J, Wilson-Kubalek EM, Milligan RA, Müller U, Kachar B. 2007. Cadherin 23 and protocadherin 15 interact to form tip-link filaments in sensory hair cells. *Nature* **449**:87–91. doi:10.1038/nature06091

Kremer JR, Mastronarde DN, McIntosh JR. 1996. Computer visualization of three-dimensional image data using IMOD. *J Struct Biol* **116**:71–76. doi:10.1006/jsbi.1996.0013

Maeda R, Kindt KS, Mo W, Morgan CP, Erickson T, Zhao H, Clemens-Grisham R, Barr-Gillespie PG, Nicolson T. 2014. Tip-link protein protocadherin 15 interacts with transmembrane channel-like proteins TMC1 and TMC2. *Proc Natl Acad Sci U S A* **111**:12907–12912. doi:10.1073/pnas.1402152111

Marquis RE, Hudspeth AJ. 1997. Effects of extracellular Ca2+ concentration on hair-bundle stiffness and gating-spring integrity in hair cells. *Proc Natl Acad Sci* **94**:11923–11928. doi:10.1073/pnas.94.22.11923

Mastronarde DN, Held SR. 2017. Automated tilt series alignment and tomographic reconstruction in IMOD. *J Struct Biol*, Electron Tomography **197**:102–113. doi:10.1016/j.jsb.2016.07.011

McPherson DR. 2018. Sensory Hair Cells: An Introduction to Structure and Physiology. *Integr Comp Biol* **58**:282–300. doi:10.1093/icb/icy064

Metlagel Z, Krey JF, Song J, Swift MF, Tivol WJ, Dumont RA, Thai J, Chang A, Seifikar H, Volkmann N, Hanein D, Barr-Gillespie PG, Auer M. 2019. Electron cryo-tomography of vestibular hair-cell stereocilia. *J Struct Biol* **206**:149–155. doi:10.1016/j.jsb.2019.02.006

Michel V, Goodyear RJ, Weil D, Marcotti W, Perfettini I, Wolfrum U, Kros CJ, Richardson GP, Petit C. 2005. Cadherin 23 is a component of the transient lateral links in the developing hair bundles of cochlear sensory cells. *Dev Biol* **280**:281–294. doi:10.1016/j.ydbio.2005.01.014

Michel V, Pepermans E, Boutet de Monvel J, England P, Nouaille S, Aghaie A, Delhommel F, Wolff N, Perfettini I, Hardelin J-P, Petit C, Bahloul A. 2020. Interaction of protocadherin-15 with the scaffold protein whirlin supports its anchoring of hair-bundle lateral links in cochlear hair cells. *Sci Rep* **10**:16430. doi:10.1038/s41598-020-73158-1

Mulhall EM, Ward A, Yang D, Koussa MA, Corey DP, Wong WP. 2021. Single-molecule force spectroscopy reveals the dynamic strength of the hair-cell tip-link connection. *Nat Commun* **12**:849. doi:10.1038/s41467-021-21033-6

Oroz J, Galera-Prat A, Hervás R, Valbuena A, Fernández-Bravo D, Carrión-Vázquez M. 2019. Nanomechanics of tip-link cadherins. *Sci Rep* **9**:13306. doi:10.1038/s41598-019-49518-x

Pettersen EF, Goddard TD, Huang CC, Meng EC, Couch GS, Croll TI, Morris JH, Ferrin TE. 2021. UCSF ChimeraX: Structure visualization for researchers, educators, and developers. *Protein Sci Publ Protein Soc* **30**:70–82. doi:10.1002/pro.3943

Pickles JO, Comis SD, Osborne MP. 1984. Cross-links between stereocilia in the guinea pig organ of Corti, and their possible relation to sensory transduction. *Hear Res* **15**:103–112. doi:10.1016/0378-5955(84)90041-8

Powers RE, Gaudet R, Sotomayor M. 2017. A Partial Calcium-Free Linker Confers Flexibility to Inner-Ear Protocadherin-15. *Struct Lond Engl 1993* **25**:482–495. doi:10.1016/j.str.2017.01.014

Powers RJ, Roy S, Atilgan E, Brownell WE, Sun SX, Gillespie PG, Spector AA. 2012. Stereocilia Membrane Deformation: Implications for the Gating Spring and Mechanotransduction Channel. *Biophys J* **102**:201–210. doi:10.1016/j.bpj.2011.12.022

Song J, Patterson R, Metlagel Z, Krey JF, Hao S, Wang L, Ng B, Sazzed S, Kovacs J, Wriggers W, He J, Barr-Gillespie PG, Auer M. 2020. A cryo-tomography-based volumetric model of the actin core of mouse vestibular hair cell stereocilia lacking plastin 1. *J Struct Biol* **210**:107461. doi:10.1016/j.jsb.2020.107461

Sotomayor M, Weihofen WA, Gaudet R, Corey DP. 2012. Structure of a force-conveying cadherin bond essential for inner-ear mechanotransduction. *Nature* **492**:128–132. doi:10.1038/nature11590

Tang Y-Q, Lee SA, Rahman M, Vanapalli SA, Lu H, Schafer WR. 2020. Ankyrin Is An Intracellular Tether for TMC Mechanotransduction Channels. *Neuron* **107**:112-125.e10. doi:10.1016/j.neuron.2020.03.026

Tilney LG, Tilney MS, DeRosier DJ. 1992. Actin filaments, stereocilia, and hair cells: how cells count and measure. *Annu Rev Cell Biol* **8**:257–274. doi:10.1146/annurev.cb.08.110192.001353

Zheng W, Holt JR. 2021. The Mechanosensory Transduction Machinery in Inner Ear Hair Cells. *Annu Rev Biophys* **50**:31–51. doi:10.1146/annurev-biophys-062420-081842

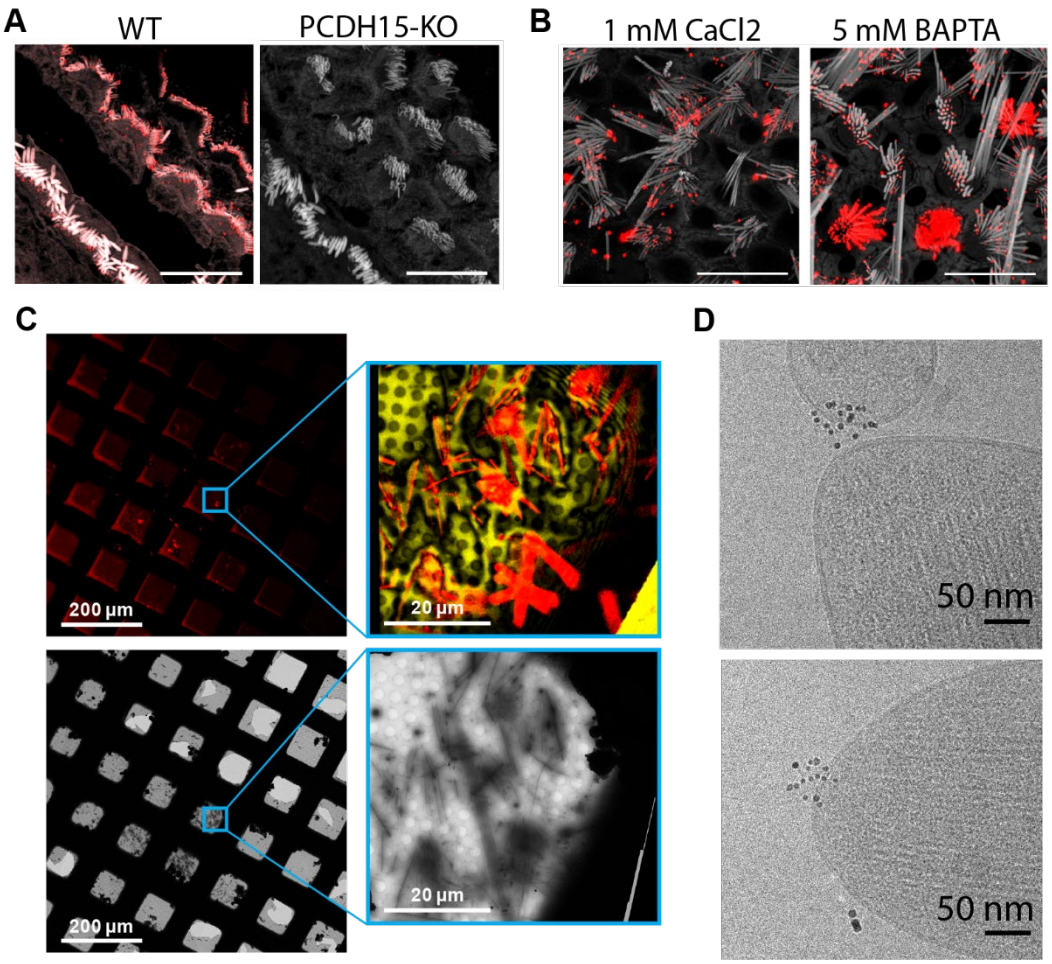

Figure 1. Cryo-EM data-collection of antibody stained stereocilia tips supported by cryo-CLEM

(A) Immunostaining of WT cochlea or PCDH15 KO with polyclonal antibody raised in rabbits against PCDH15 extracellular domain. (B) Immunostaining of WT utricle with polyclonal antibody in media containing 1mM CaCl2 or with the addition of 5mM BAPTA (C) CLEM-based screening to identify squares with thin-ice supported stereocilia. The top row shows low- and medium magnification views acquired using a cryo-light microscope. In both views SirAction fluorescence is shown in red. In the medium-magnification view laser-reflection is shown in gold. The bottom rows show the same areas as acquired in a cryo-TEM. (D) High-

565 magnification cryo-TEM micrographs of stereocilia tips stained with the anti-PCDH15 rabbit

566 polyclonal antibody, detected with a 5nm gold coupled secondary antibody.

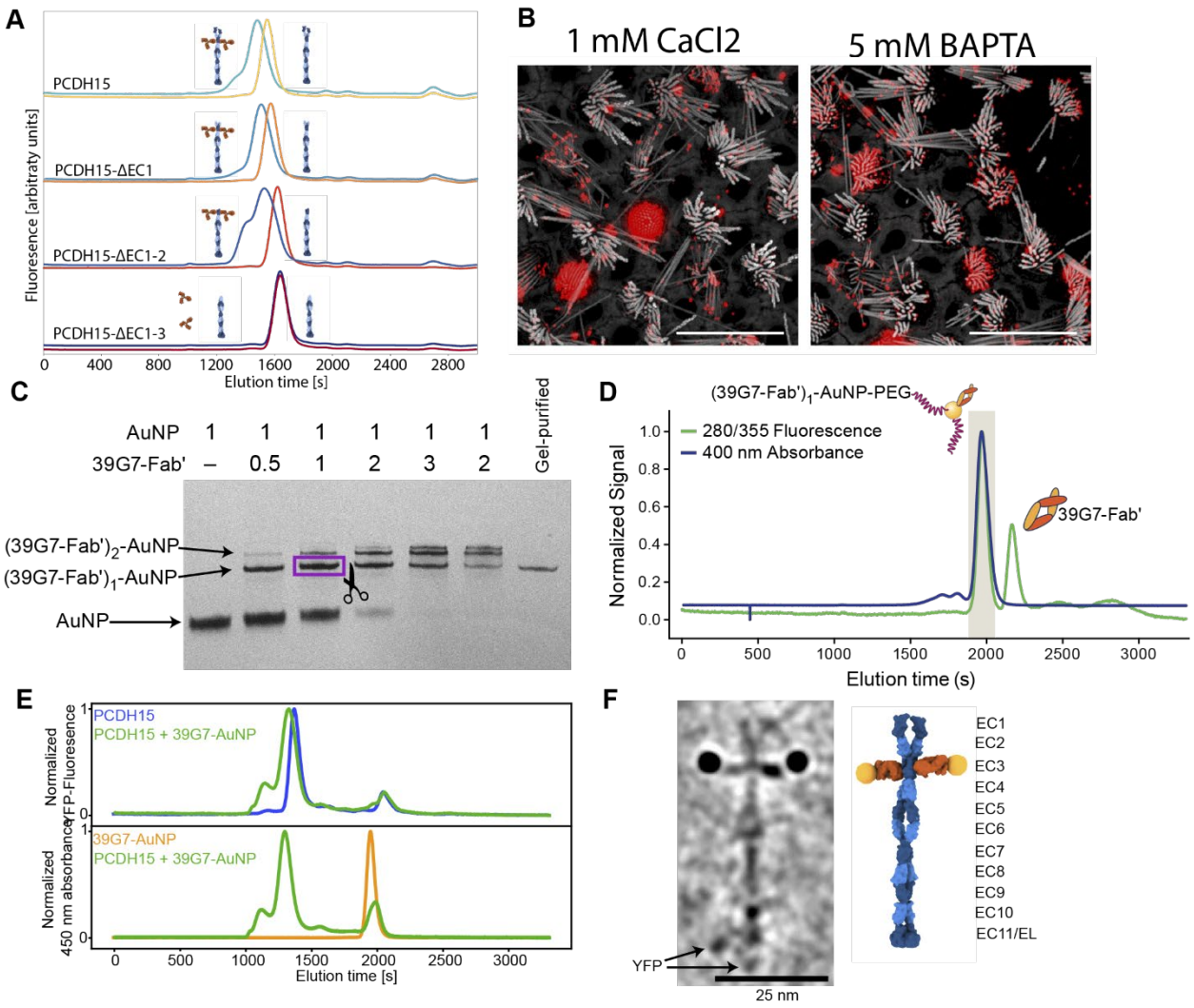

568 **Figure 2. Stoichiometric gold staining of PCDH15 using a monoclonal Fab AuNP conjugate**

569 (A) FSEC analysis of binding of 39G7 to the PCDH15 extracellular domain. 39G7 addition leads

570 to earlier elution of PCDH15 in full-length constructs and after deletion of EC1 and EC2.

571 Deletion of EC3 abolished 39G7 binding. (B) Immunostaining of WT utricle with 39G7 in media

572 containing 1mM CaCl2 or with the addition of 5mM BAPTA. (C) PAGE analysis and

573 purification of conjugation between 39G7 Fab' and a 2nm AuNP (D) SEC purification of PEG-

574 coated 39G7-Fab'-AuNP conjugates. (E) FSEC analysis of 39G7-Fab'-AuNP-PEG conjugate to

575 PCDH15 extracellular domain. (F) Cryo-TEM image of PCDH15 extracellular domain bound to

576 39G7-Fab'-AuNP-PEG conjugate together with model of the complex. In the model PCDH15 is

577 shown in blue, 39G7 Fab in orange, and AuNPs as golden spheres.

578

579

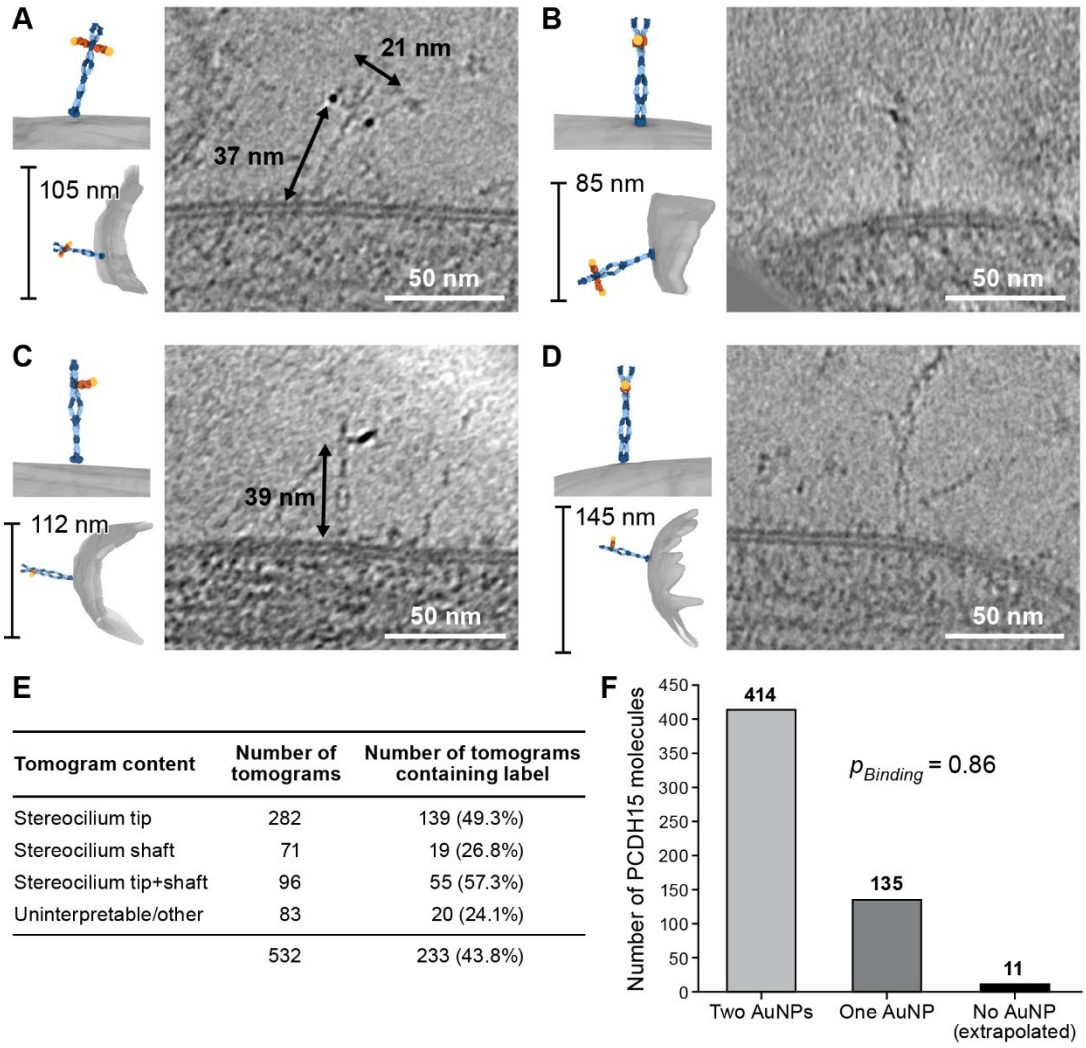

E

Tomogram content	Number of tomograms	Number of tomograms containing label
Stereocilium tip	282	139 (49.3%)
Stereocilium shaft	71	19 (26.8%)
Stereocilium tip+shaft	96	55 (57.3%)
Uninterpretable/other	83	20 (24.1%)
	532	233 (43.8%)

581 **Figure 3. 39G7-AuNP conjugate labels PCDH15 dimer in stereocilia**

582 (A-B) Representative examples of PCDH15 dimers with two bound AuNPs imaged *in situ*. (C-
583 D) Representative examples of PCDH15 dimers with one bound AuNPs imaged *in situ.* Dimeric
584 features in the PCDH15 density suggests that these molecules are PCDH15 dimers with one
585 epitope not bound to 39G7. (E) Table detailing numbers and content of collected tomograms. (F)
586 Bar chart quantifying the ratio of PCDH15 molecules labeled by one or two AuNPs. Assuming
587 that AuNPs bind independently to the two epitopes in the PCDH15 dimer results suggests that
588 86% of all epitopes were labeled and only 2% of PCDH15 molecules were unlabeled.

589

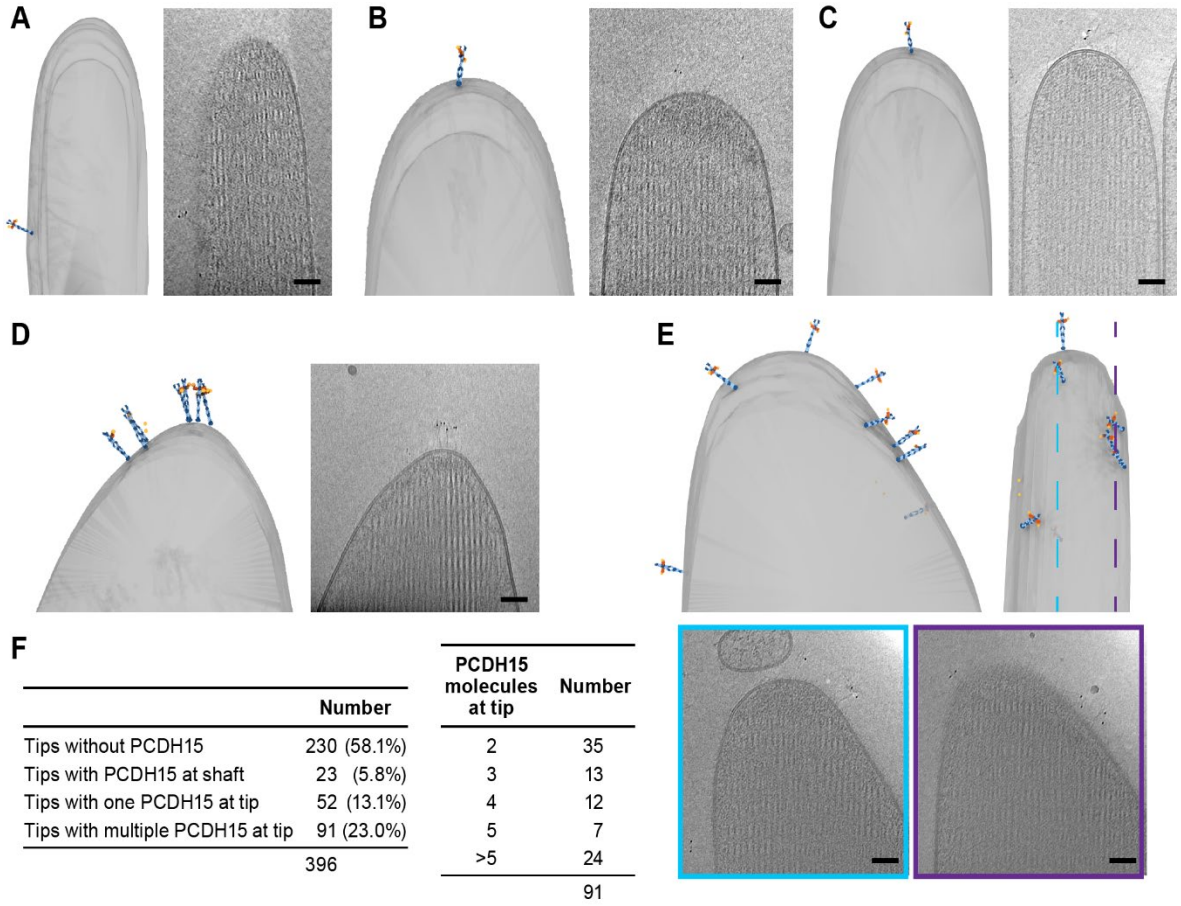

	Number
Tips without PCDH15	230 (58.1%)
Tips with PCDH15 at shaft	23 (5.8%)
Tips with one PCDH15 at tip	52 (13.1%)
Tips with multiple PCDH15 at tip	91 (23.0%)
	396

PCDH15 molecules at tip	Number
2	35
3	13
4	12
5	7
>5	24
	91

591 **Figure 4. Stereocilia tips frequently harbor more than one copy of PCDH15**

592 (A) Representative example of stereocilia tip with PCDH15 molecule only found in adjacent
593 shaft. (B-C) Representative examples of stereocilia tips with one copy of PCDH15 at tip. (D-E)
594 Representative examples of stereocilia tips with multiple copies of PCDH15 at tip. (F) Table
595 detailing number of imaged stereocilia tips and distribution of PCDH15 molecules found at the
596 tip.

597

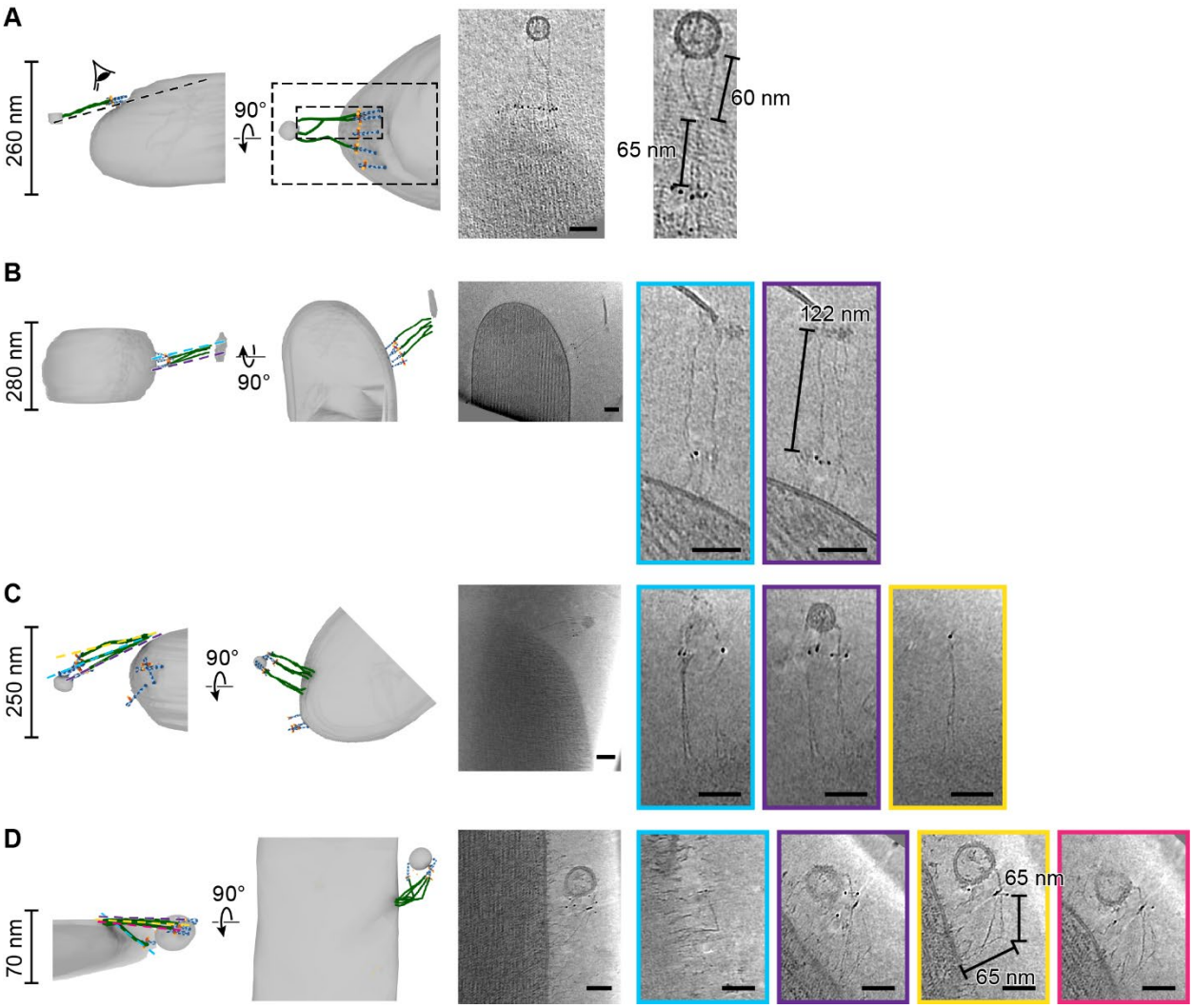

Figure 5. PCDH15/CDH23 tetramers are found in clusters

On the left side of each panel the tomogram annotation is shown from the side and from top. On the sideview ice thickness is indicated. To the right of the annotation is a projection of the cluster density in context of the stereocilium. Further to the right are detailed slices of the electron density. The angle and position of each slice is indicated in the sideview of the tomogram annotation. Scale bars correspond to 50nm. (A-B) Representative tomograms showing PCDH15/CDH23 heterotetramers with PCDH15 at tip of stereocilium and CDH23 in lipid fragment. (C-D) Representative tomograms showing PCDH15/CDH23 heterotetramers with CDH23 in side of stereocilium and PCDH15 in lipid fragment.

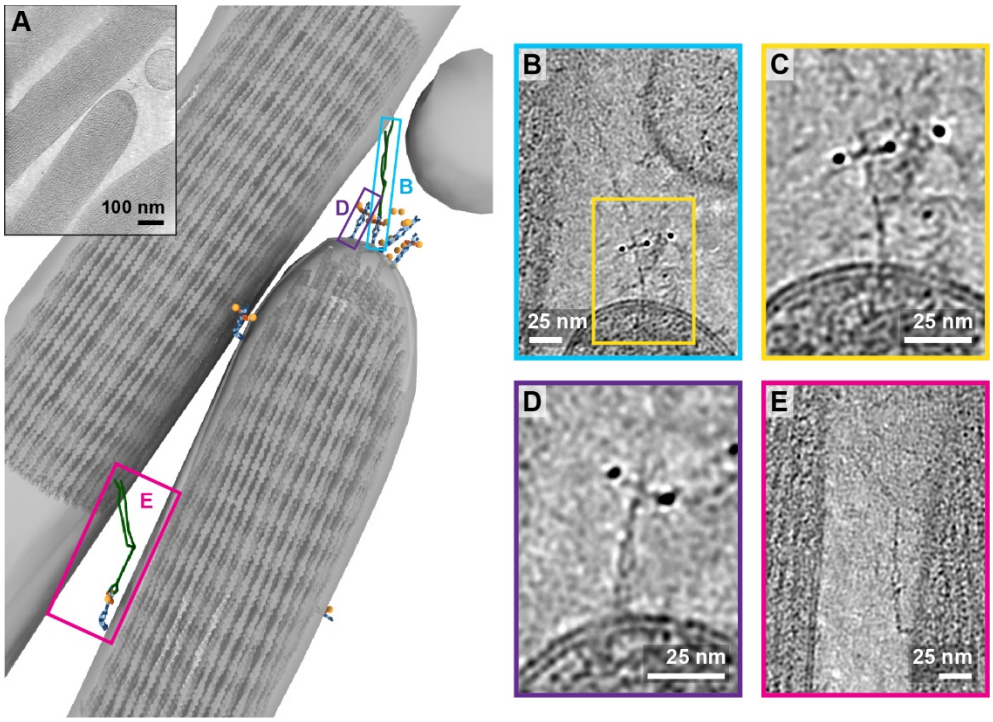

Figure 6. Tomogram containing intact tip-link

(A) Annotation of tomogram showing a putative intact tip-link. The inset at the top left shows a projection of the tomogram. (B) Closeup view of putative tip-link density in the tomogram. (C) Closeup of PCDH15 density in tip-link. (D) Close-up of PCDH15 molecule at tip not bound to CDH23. (E) Close-up of PCDH15/CDH23 heterotetramer in the stereocilia shaft region. PCDH15 has a 90° bend between EC9 and EC10.

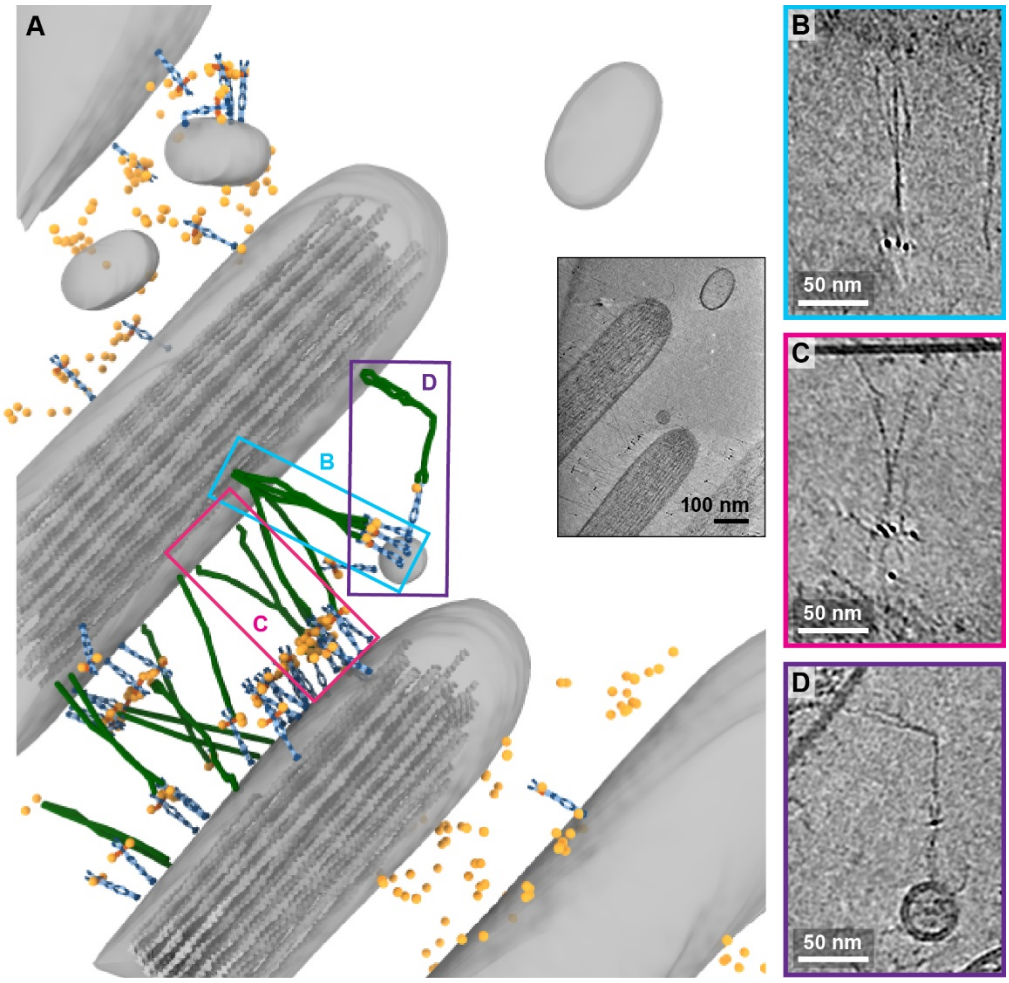

Figure 7. Tomogram depicting lateral links containing PCDH15 in small stereocilia

(A) Annotation of tomogram showing developing stereocilia including PCDH15/CDH23 'lateral links'. The inset at the bottom right shows a projection of the tomogram. (B-C) Closeup of CDH23 molecules clustering together into single strand. (D) Closeup of CDH23 molecule with distinct bend half-way between N- and C-terminal end.

Supplementary Materials

Movie S1. Tomogram of recombinant PCDH15 extracellular domain in complex with 39G7-AuNP conjugate.

Movie S2. Tomogram of stereocilium displaying a PCDH15 dimer with two bound 39G7-AuNP conjugates, also depicted in Figure 3A.

Movie S3. Tomogram of stereocilium displaying a PCDH15 dimer with two bound 39G7-AuNP conjugates, also depicted in Figure 3B.

Movie S4. Tomogram of stereocilium displaying a PCDH15 dimer with one bound 39G7-AuNP conjugates also depicted in Figure 3C.

Movie S5. Tomogram of stereocilium displaying a PCDH15 dimer with one bound 39G7-AuNP conjugates, also depicted in Figure 3D.

Movie S6. Tomogram of stereocilium tip with a single PCDH15 dimer in the shaft region of the tip, also depicted in Figure 4A.

Movie S7. Tomogram of stereocilium tip with a single PCDH15 dimer at the apex of the tip, also depicted in Figure 4B.

Movie S8. Tomogram of stereocilium tip with a single PCDH15 dimer at the apex of the tip, also depicted in Figure 4C.

Movie S9. Tomogram of stereocilium tip with a cluster of multiple PCDH15 dimers at the apex of the tip, also depicted in Figure 4D.

Movie S10. Tomogram of stereocilium tip with multiple PCDH15 dimers scattered around the tip, also depicted in Figure 4E.

Movie S11. Tomogram of stereocilium tip containing multiple PCDH15 dimers connected to putative CDH23 filaments in a lipid vesicle, also depicted in Figure 5A.

Movie S12. Tomogram of stereocilium tip containing multiple PCDH15 dimers connected to putative CDH23 filaments in a lipid membrane fragment, also depicted in Figure 5B.

Movie S13. Tomogram of a stereocilium tip containing multiple putative CDH23 filaments connected to PCDH15 dimers in a lipid vesicle, also depicted in Figure 5C.

Movie S14. Tomogram of a stereocilium shaft containing multiple putative CDH23 filaments connected to PCDH15 dimers in a lipid vesicle, also depicted in Figure 5D.

Movie S15. Tomogram of a stereocilium tip and a stereocilium shaft containing a PCDH15 dimer in the stereocilium tip that is connected to a putative CDH23 filament in the neighboring stereocilium shaft. The tip also contains PCDH15 dimers not bound to CDH23. An additional putative PCDH15/CDH23 complex is connecting the two stereocilia in the shaft region. Also depicted in Figure 6.

Movie S16. Tomogram of stereocilia connected by tens of PCDH15/CDH23 complexes. Noteworthy complexes, that include apparent interaction between CDH23 dimers, as well as bends in the CDH23 dimer are highlighted. Also depicted in Figure 7.